Phenotypic plasticity in coral skeletal features: Molecular signatures from DNA methylation and transcriptional interaction networks

Running Title: Induced phenotypic plasticity and methylome repatterning.

Kelly Gomez-Campo[1*], Robersy Sanchez[1], Isabel Martínez-Rugerio[1], Xiaodong Yang[1], Tom Maher[1], C. Cornelia Osborne[1], Susana Enriquez[3], Iliana B. Baums[1,4], Sally A. Mackenzie[1,2], Roberto Iglesias-Prieto[1*]

[1]Department of Biology, The Pennsylvania State University, University Park, PA 16802, USA

[2]Department of Plant Science, The Pennsylvania State University, University Park, PA 16802, USA

[3]Unidad Académica de Sistemas Arrecifales Puerto Morelos, Instituto de Ciencias del Mar y Limnología, Universidad Nacional Autónoma de México, 77580, México

[4] Helmholtz Institute for Functional Marine Biodiversity, Ammerlaender Heerstrasse 231, 26129 Oldenburg, Germany

*Correspondence to: kjg27@psu.edu (K.G.C.); rzi3@psu.edu (R.I.P).

Author contributions: R.I.P., I.B.B., S.A.M. and K.G.C. conceived and designed the experiments. K.G.C performed the experiments, integrated, and analyzed the data. I.B.B., S.A.M., R.S., and X.Y. contributed to genomic-epigenomic analysis and interpretations. S.A.M. and R.S. to Methyl-IT and biological network analyses. R.I.P. and S.E. to phenotypic descriptions interpretation. I.M.R. assisted in field work and phenotypic descriptions. T.M. assisted in methylation computational work. C.C.O. assisted in laboratory and gene expression computational work. K.G.C and R.I.P. wrote the manuscript. K.G.C, S.E., I.B.B, S.A.M., R.I.P. reviewed and edited the manuscript. Funding acquisition: R.I.P., I.B.B., S.A.M. All authors approved the manuscript.

Competing Interest Statement: Authors declare no competing interests.

Classification: Biological Sciences, Ecology, Genetics, Physiology

Keywords: Phenotypic plasticity, DNA methylation, gene expression, biological networks, biomineralization.

This PDF file includes:

Main Text
Figures 1 to 6

Abstract

Acclimation through phenotypic plasticity represents a more rapid response to environmental change than adaptation and is vital to optimize organisms' performance in different conditions. Generally, animals are less phenotypically plastic than plants, but reef-building corals exhibit plant properties. They are light-dependent with a sessile and modular construction that facilitates rapid morphological changes within their lifetime. We induced phenotypic changes by altering light exposure in a reciprocal transplant experiment and found that coral plasticity is a colony trait emerging from comprehensive morphological and physiological changes at the local level. Plasticity in skeletal features optimized coral light harvesting and utilization and paralleled with significant methylome and transcriptome modifications. Network-associated responses resulted in the identification of hub genes and clusters associated to the change in phenotype: inter-partner recognition and phagocytosis, soft tissue growth and biomineralization. Furthermore, we identified hub genes putatively involved in animal photoreception-phototransduction. These findings fundamentally alter our understanding of how cnidarian invertebrates repattern the methylome and adjust a phenotype, revealing an important role of light sensing by the coral animal to optimize photosynthetic performance of the symbionts.

Significance Statement

Stony corals shape the benthic topography of the ocean by the net accumulation of calcium carbonate, engineering biodiversity hotspots that provide food security, livelihood opportunities, and protection from coastal erosion worldwide. Corals optimize growth through morphological plasticity, however, genomic and epigenomic underpinnings of such plasticity are largely unknown. We applied comprehensive biometrics, machine learning to identify divergent methylation, and methylome-transcriptome-derived network analyses. We revealed an extraordinary number of hub genes likely to be integral to morphologic plasticity. Accordingly, DNA methylation may represent an important mechanism facilitating the evolution of the biomineralization process. The integration of methylation and transcriptional information makes significant inroads in the identification of networks underpinning phenotypic changes and provides a roadmap for studies of non-model organisms.

Main Text

Introduction

The modification of an organism's physical features (phenotype) through development and growth is affected by the interaction of gene expression (genotype) with environmental cues. This capacity for phenotypic plasticity allows organisms to optimize their physiological performance under different environmental conditions (1–3). While most organisms exhibit some degree of plasticity, the sessile condition of plants prevents movement to new environments if conditions become unfavorable. Consequently, they have evolved broad plasticity in their physical characteristics, such as leaf size or shape, root architecture or reproductive behaviors, to cope with changing environments and maintain optimal light harvesting (4). Animals generally exhibit far less plasticity than plants; except for reef-building corals. With similar life-histories to plants, their colonies display high levels of morphological plasticity.

Corals are modular, sessile organisms responsible for the net accumulation of calcium carbonate in coral reefs. The power to calcify is the result of animals acquiring photosynthetically-fixed carbon through an obligate symbiosis with dinoflagellates (or microalgae) (family Symbiodiniaceae) (5–8). This means that corals, much like plants, make their living from light capture. The metabolic integration is such that coral skeletons evolved to be efficient light collectors (9) with skeletal morphology adjusted in response to depth-dependent light availability (10). It is, therefore, not surprising that corals exhibit molecular signatures for perceiving and responding rapidly to changes in light availability.

While observed phenotypic plasticity is shaped by the interaction between genomes and environments, the role of epigenomes in this plasticity has captivated the interest of biologists. Phenotypic adjustments induced by environmental cues and gene expression may be influenced by chromatin factors like DNA cytosine methylation, a dynamic feature of many eukaryotic genomes, including plants, animals, and fungi. DNA methylation is a process where methyl groups are added to cytosine bases of the DNA molecule and, in association with histone modifications, modify chromatin conformation (11, 12). High-density methylation within promoter regions can silence genes, whereas lower-density intragenic methylation repatterning can influence alternative splicing activity, leading to changes in an organism's phenotype (13, 14). This is a reversible process influenced by environmental conditions, hence allowing phenotypic plasticity to occur (15, 16). Moreover, methylation repatterning accompanies chromatin response to environmental changes without altering the DNA sequence and with the potential for heritable transmission. The repatterning is generally associated with other epigenetic effects such as histone modifications and changes in noncoding RNA. These methylome modifications can be assayed at single nucleotide resolution, providing the robust datasets required for identifying responsive underlying gene networks that could explain phenotypic adjustments (17–22).

DNA methylation is evolutionarily ancient; however, its distribution and functions are diverse, debatable, or unknown among taxa. In plants, phenotypic plasticity and its heritability has been associated with changes in DNA methylation patterns (15, 16), but the functional significance in coral phenotypic plasticity is still tenuous. Several studies have associated coral DNA methylation with plasticity (23–30), with whole-genome bisulfite sequencing (WGBS) contributing to single base-pair resolution (27). However, WGBS data analysis can be challenging due to the highly dynamic features of methylome datasets. This stochasticity has complicated discrimination of treatment-associated signal from natural background variation, and the understanding of treatment-associated phenotypic adjustments with methylome modifications (17, 22). As advances in computational biology demonstrate the effect of single cytosine changes in phenotypic responses, novel methods have been addressing challenges in conventional methodologies (17–22). One approach to discriminate treatment-associated differential methylation is to incorporate signal detection and machine learning (18, 20–22, 31) with MethylT (R package Methyl-IT 0.3.1.2, (21)). The approach treats methylation data as probability distributions, permitting variation within

multiple control samples to be subtracted from the treatment datasets to discriminate treatment-specific variation. Machine learning then permits validation of treatment association with over 98% confidence. Further validation of this approach is accomplished, in models like Arabidopsis, with incorporation of mutations in the RNA-directed DNA methylation pathway (18). However, the approach is especially valuable in non-model systems where changes cannot be confirmed with targeted mutation(s). The association between phenotype change and treatment-associated methylome modification is informative in understanding the underlying molecular features of the phenotypic change by directly identifying responsive gene networks (18, 20–22, 31).

To examine the phenotype to methylome association, we conducted a reciprocal transplant experiment to induce light-mediated phenotypic responses in the reef-building Elkhorn coral *Acropora palmata* and investigated DNA methylation and transcriptional responses potentially responsible for plasticity. Extensive biometrics revealed not only changes in coral tissue pigmentation and metabolic rates but also in skeletal morphology after five weeks. This skeletal remodeling was accompanied by intragenic methylome repatterning, discovered by signal detection with machine learning-based analysis. We further integrated differentially methylated (DMG) and expressed (DEG) gene datasets to elucidate how light responses integrate into gene regulatory networks controlling functional traits. By exploring the resulting hub genes and gene clusters, we were able to predict functional associations with observed phenotype changes and identify markers of plasticity in reef-building corals. Moreover, our results contribute to emerging evidence that epigenetics contribute to the machinery that can alter DNA structure during skeletal remodeling in metazoans.

Results and Discussion

Corals exploit intra-colonial environmental differences through plasticity

The branching coral *Acropora palmata* is the dominant reef-builder on shallow, wave-exposed Caribbean reefs. Colonies exhibit tree-like morphologies with strong intra-colonial light gradients ranging from 3 to 100% of sub-superficial irradiance (E_s). In our experiment, we quantified intra-colonial phenotypic plasticity by measuring traits from High Light (HL) surfaces (fragments from upperside surfaces of branches, n = 12) exposed to 70% of E_s and Low Light (LL) surfaces (fragments from underside surfaces of branches, n =12) exposed to 3-7% of E_s (**Fig. 1A, Table 1**). Structural, optical, and physiological traits of HL and LL fragments releveled two distinct phenotypes. HL phenotypes had significantly greater total polyp density (**Fig. 1F**), density of taller corallites (**Fig. 1G**), total host protein (**Fig. 1H**) and algal density (**Fig 1I**). Surfaces with taller corallites can favor the formation of internal light gradients, increase levels of pigment self-shading, and reduce the proportion of polyp-surface exposed to the external high-light levels (9, 32). In contrast, LL phenotypes showed a small number of short corallites that can facilitate the lateral spread of light.

We expected these differences in skeletal features to affect how corals collect and utilize light for colony growth. To disentangle this, we used algal symbiont density, chlorophyll *a* (chl*a*), host soluble proteins, and *in vivo* light absorption of the intact coral tissue (**Table S1**) to describe light absorption efficiency of HL and LL phenotypes. We estimated three optical traits: a^*_{Chla} (m^2 mg Chla^{-1}), which describes the holobiont's efficiency to absorb light (33), a^*_{sym} (m^2 sym^{-1}) that describes *in hospite* light absorption efficiency of the algal symbionts, and a^*_M (cm^2 mg $protein^{-1}$) indicative of the potential return for the host (mass) of the energy absorbed (34, 35) (**Table S1**). We detected less algal cell densities (**Fig. 1I**) but more chl*a* per cell in LL phenotypes (**Fig. 1J**), and opposite traits in HL phenotypes. This resulted in equal chl*a* concentration in both HL and LL phenotypes (**Fig 1K**). These findings contradict the assumption that more light always induces lower pigmentation in multicellular photosynthetic organisms and confirms the ability of coral skeletal features to rewire the algal light environment. Conversely, a^*_{Chla} showed that both phenotypes of the coral colony are equally efficient in absorbing light (**Table S1**), a response reached by adjusting skeletal features.

A. palmata exploits a wide range of light environments without changing its symbiont species (*Symbiodinium 'fitti'*), (36) in contrast to other reef-building corals (37). Instead, *A. palmata* colonies fine-tune structural traits; algal density, chl*a* density, and skeletal morphology (**Fig. 1).** This mechanism minimizes "pigment packing" in underside surfaces in response to LL conditions, resulting in light collectors as efficient as those of HL surfaces. Although photosynthesis is more active on upper side surfaces (**Fig. 1N**), the ratio of photosynthesis/respiration (P/R = 3), photosynthetic efficiency (**Fig. 1L**) and minimum quantum requirement (**Table S1**) were similar in both sides of branches. These observations further highlight the ability of *A. palmata* to optimize light absorption and utilization through plasticity as a central strategy to exploit the strong intra-colonial light gradient and maximize colony productivity for growth.

Induced morphological plasticity with reciprocal transplants

A. palmata frequently reproduce asexually via branch fragmentation, a result of physical disturbance (*i.e.* waves and storms) (38). Branches are often turned upside down when they land on the benthos. Fragmentation thus induces strong and rapid changes in light regimes, where survival is dependent on their successful acclimatization to the new light conditions. Presumably, upper and underside branch surfaces interchange phenotypes through acclimation to new light regimes. We took advantage of this life history trait to induce plasticity by altering light exposure in a reciprocal transplant experiment (see Methods, **Fig. 2A**). Coral fragments from three colonies representing three distinct genets (detected with Standard Tools for Acroporid Genotyping STAGdb (64)) were manipulated, so that HL phenotypes (n = 21) and LL phenotypes (n = 21) experienced unchanged light fields, and treated fragments were switched to the opposite light condition HL→LL (High Light to Low Light, n = 21) and LL→HL (Low Light to High Light, n = 21) (**Fig. 2A**). Within 5 weeks, treated coral fragments significantly adjusted their phenotype. The acclimation was gradual (tracked by visual inspection), and transplants became increasingly similar in morphology to coral surfaces of the destination light condition (**Fig. 2C, Fig. S4**), comparable to what is observed when coral colonies are transplanted along depth gradients (10). Pressure over photosystem II (Q_m), metabolic rates and visual growth indicated that corals acclimated successfully to the destination light conditions (**Fig. 2B, C, Table S1**). Interestingly, a^*_{Chla}, the holobiont's efficiency to absorb light, indicated that fragments may continue changing pigmentation and skeletal features to fully optimize performance (**Fig. 2D, E**). Nonetheless, most significant changes were observed in skeletal features (taller corallites per area), polyp density and the balance between chl*a* density and symbiont density (**Fig. 2, Table S1**). Significant differences were found among the 4 group conditions (R = 0.336, P<0.001, **Fig. S5**), suggesting a response driven by light-mediated phenotypes and not the genet (R = 0.188, P> 0.05).

Phenotypic plasticity was induced by altering ~80% of light availability (~18 mol quanta m^{-2} day^{-1}). These were drastic changes that are nevertheless commonly experienced by coral species during their life cycle. Whole colony metabolic performance is optimized by adjustments at the module (polyp) level for resource acquisition. Similarly, phenotypic plasticity in plants results from a local response (*e.g.* of shaded branches) which optimizes light harvesting and utilization for growth (39). While corals are colonial animals, and each polyp (module) is akin to an individual organism, a coral's response to the light environment should consider the integrated response to local conditions experienced by local modules. Accordingly, modular plasticity may be one evolving trait under selection, as has been suggested for plants (39).

Reading the methylome with Methyl-IT: Light-mediated methylome repatterning

Following induced light-mediated phenotypic plasticity, we investigated DNA methylome response to coral group conditions (n = 8 per group condition). With WGBS (30X coverage), we documented methylation of the *A. palmata* genome. We identified CpG context methylation (~14%) to be higher in the *A. palmata* than in any other invertebrate (27, 40). We detected insignificant levels of methylation in CHG or CHH context (<0.6%) (H = A, T, or C) (**Fig. 3A**), and CpG methylation was prevalent in genic regions (**Fig. 3B**) as previously reported in other coral species (23, 27, 28).

To associate the observed coral phenotypic plasticity with high-resolution DNA methylome variation, we used a signal detection-machine learning approach (R package Methyl-IT 0.3.1.2) (21), designed to discriminate methylation signal induced by environmental variation at individual cytosine positions (19, 21, 41). We assessed gene-associated, differentially methylated positions (DMPs) with no regard to methylation density, context, or directionality (hypo/hypermethylation) (Methods, **Fig. 3C**). Parallel analysis of DMP variation within control samples allowed discrimination of treatment-associated DMPs and their classification on the basis of hierarchical clustering (HC) and principal component analysis (PCA) (Methyl-IT), which enabled an unbiased view of methylome repatterning (**Fig. 3D**). There was significant separation of control and treatment samples, indicating that light-mediated methylome modifications were driving the first two principal components. Genes with the strongest discriminatory power from PC-scores in PC1 were associated with cell cycle, extracellular matrix (ECM), regulation of transcription and transduction, and biomineralization (**Table S2)**.

Agnostic biological network analysis with WGCNA: Network-based integration of DMG and DEG datasets

Significant coral phenotypic changes and gene-associated methylome repatterning warranted deeper investigation to uncover functional relationships with gene expression. We first identified DMGs (Methyl-IT 0.3.1.2) based on statistically significant differences in DMP counts from treated corals relative to control groups (**Fig. S2**). RNA-sequencing was carried out on the same samples used for WGBS, with DEGs identified (DESeq2 3.12.0.) via pairwise comparison between control and treatment groups. A total of 32 methylomes and 32 transcriptomes were analyzed with a range of 861 – 2255 DMGs and 1334 – 6479 DEGs detected (**Fig. S6**). We used a network-based approach to integrate the information, which provided us with a collection of nodes and edges representing putative gene interactions (42). Since network-based analyses can be influenced by the available annotation for a given species, we performed a weighted correlation network analysis of coral gene expression and methylome modification (**Fig. S2**). To understand the interaction between the change in methylomes (n = 32) and transcriptomes (n = 32), we combined DMG and DEG datasets to one large dataset genes/coordinates. Dimensionality was reduced with HC (**Fig. 4A**), PCA and a linear discriminant analysis. We assigned gene discriminatory power from PC-scores (gene-score) (**Fig. S7**). The network was built in R-package Weighted Gene Correlation Network Analysis (WGCNA 1.71) (43), with visualization and statistical analysis in Cytoscape 3.8.2 (19). Network's centrality measures, edge weight, and node PC-scores were included in clustering analyses to identify putative central regulators or hub genes. Hub loci are critical network components, with loss or mutation predicted to cause breakdown of the network or lethality to the organism (19, 42).

Methylome-transcriptome-derived gene network information revealed an extraordinary number of hub genes likely to be integral to morphologic plasticity in symbiotic corals. General biological processes included visual and sensory perception, growth and immunity, including carriers, transporters and receptors. Two main cluster categories were identified (**Fig. 4B**). A Type I subnetwork (**Fig. 4C**) showed genes with strong gene-gene interaction (edges with strongest correlation weights), denotating genes with similar contribution to the change in phenotype. The main sub-network under this category was enriched in Extracellular matrix (ECM) gene products, collagen-like domains, signaling activity, cell-cell adhesion and EGF-domains, putatively associated with soft tissue growth and biomineralization (R-HSA-2022090, R-HSA-1474244, R-HSA-1474290, R-HSA-2022090, R-HSA-388844, R-HSA-8849932). 139/199 genes in this subnetwork were found to be differentially methylated, highlighting the influence of methylation to changes in coral skeletal growth. Interestingly, we observed low gene-score values in this cluster, meaning that individually each gene carries small proportion of the whole phenotypic variance. Seemingly, these genes were co-methylated to give rise to a quantitative cumulative effect on phenotypic variation among treatments, leading to the change in growth pattern, but with low discriminatory power individually.

Subnetworks Type II represented critical genes with the strongest discriminatory power, denoting hub genes with strongest contribution to the change in phenotype (**Fig. 4D, E)**. Accordingly, we considered these loci to be strong candidates for biomarker identification. Annotated hub genes included DEG*SLC7A2,* DEG*SLC22A13,* DEG*SLC17A6B,* DEG*PANP*, DEG*IFI30*, DEG*TRIM71*, DEG*MELC2*, DEG*ADAMTS18*, DEG*CTRC*, DMG*HECTD4*, DMG*LIPK,* DEG*TNR,* DMG*C0H691,* DMG*TRPV6,* DEG*HSP-16.2,* DEG*SUSD2,* DEG*COL6A5,* DEG*BTBD2,* DEG*CASR* DMG*GPR133,* DMG*RABL6,* DEG*PRSS27,* DEG*SSTR5,* DMG*MPDZ,* DMG*SPTAN1,* DEG*ABHD4,* DEG*COL12A1,* DEG*SPDEF,* DEG*HES4-a,* DEG*PTK7,* DEG*ASIC3* DEG*MFSD6,* DEG*COL11A1*, DMG*CHMP6*, DEG*PRDM6*, DMG*FGFR1,* DMG*TMPRSS15,* DMG*TMPRSS11D,* DEG*B3GAT3*.

Predicted biological networks: network-associated responses from DMGs

We further aimed to investigate gene interactions in available experimental data by consulting pathways from curated databases (44, 45) to identify predicted networks (see Methods; **Fig. S2**). With the set of DMGs as input in *stringApp* (Cytoscape 3.8.2), we built a baseline network and performed clustering analyses (with network centrality measures). Independent of the destination light condition and genet, enriched function categories were posttranscriptional protein variants (kw-0621 polymorphism, kw-0025 alternative splicing, kw-0597 phosphoprotein), cytoskeleton proteins (kw-0206), calcium-dependent proteins (kw-0106 calcium), growth associated proteins (kw-0131 cell cycle, kw-0965 cell-junction), and phagocytosis (kw-0966 cell projection) (**Fig. S8**). A common feature of main candidate hub genes (**Fig. S8**, *ATR, PIF1, FANCD, SIRT1*) was DNA damage-repair-response (DRR), a mechanism regulated by chromatin conformation. Chromatin remodeling complexes, at the core of DRR (46), are essential in DNA methylation patterning (47).

We used the set of DEGs to run the same network analyses separately (**Fig. S9**). However, we found significant lower values of node Eigenvector of centrality (**Fig. S10**). This limited the identification of hubs from gene expression data alone.

Predicted biological networks: network-associated responses from DMGs and DEGs.

The identification of key regulators in DMG sub-networks led us to investigate integrated DMG and DEG networks in available experimental data and pathways from curated databases (44, 45). We detected sub-networks of hub genes contributing to phenotypic changes and associated cellular processes, including inter-partner recognition and phagocytosis, regulation of host-symbiont biomass, and calcification (reviewed in (48)). Sub-networks aligned with these processes, independent of the destination light conditions and genet, and generally targeting the same enriched categories, pathways, or protein families (**Fig. 5, Fig. S11-S14**). Network topology and node hierarchy based on Eigenvector od Centrality suggested a general DMG-DEG interplay targeting key regulators (hubs) and triggering a cascade of responses, evident when source-sink nodes (**Fig. 5A** *CEP290*; **Fig. 5B** *THBS1*, *PTK2*, *SOX9*; **Fig. 5C** *RAB1A*; **Fig 5D** *ANAPC1*) interacted with strongly connected clusters.

Cells have mechanisms to detect specific environmental signals to transduce and trigger the appropriate responses. We identified a symbiont-independent photoreception-phototransduction sub-network (**Fig. 5A**, 51 nodes and 139 edges) potentially involved in animal sensing of a light stimulus (p-Cluster I). Network Enrichment Analysis (NEA) yielded mainly cilium assembly (GO.0060272, 19 enriched genes, FDR < 0.001). The putative hub gene DMG-DEG*SPTAN1* interacted with DMG*CEP290* and a transcriptional non-hub cluster (*USH2A, CRB1, EYS, MYO3A*) involved in phototransduction-reception. Interestingly, this sub-network further interacted with growth and calcification sub-networks (**Fig. 5B)**. Previous work has elucidated the role of light in the coral animal independent symbiont metabolism. It was found that enhanced coral calcification but not photosynthesis occurs under blue light exposure (49), and evidence suggests a light-mediated electrical potential in coral epithelia (50). Moreover, Cnidaria constitutes the earliest branching phylum containing a well-developed visual system. Some jellyfish, like Cubozoa, have camera-type eyes with photoreceptor cells that are more similar to vertebrate than to invertebrate eyes (51). These findings suggest that coral animal photoreception-transduction is implicated in changes in

growth pattern and skeletal features, although the role of photoreception-associated proteins is yet to be explored.

Consistent with significant changes in coral skeletal features for the optimization of light harvesting and utilization, we identified a coral growth and biomineralization sub-network (**Fig. 5B**, 86 nodes and 200 edges) that revealed NEA categories related to ECM proteins (KW-0272, 18 enriched genes, FDR < 0.001), cell-cell adhesion (KW-0130, 14 enriched genes, FDR < 0.001) and EGF-domains (KW-0245, 13 enriched genes, FDR < 0.001) as most prominent. From the sub-network of hub genes, integrin and spectrins interacted with glycoproteins and lipoproteins ($_{DMG}$*PTK2*, $_{DMG\text{-}DEG}$*THBS1*, and $_{DMG}$*LRP5*) involved in coral biomineralization (52–54). Thrombospondin has previously been suggested for its role in biomineral remodeling (55). Consistent with this network topology, an important transcriptional interaction identified was SOX9, a transcription factor (TF) with a role in skeletal development. Associated nodes involved TFs $_{DEG}$*HIF1A*, $_{DEG}$*HOPX*, and $_{DEG}$*FOXL1*, with the receptor protein $_{DEG}$*NOTCH2* up regulated in this transcriptional interaction (independent of the destination light condition). All hub genes interacted with a strongly connected cluster of collagen-like domains that was mainly transcriptional and up-regulated when transplanted to HL, while down-regulated when transplanted to LL. Collagen plays a structural role in the skeletal organic matrix (SOM), and presence of SOM in calcifying organisms appears to be a prerequisite for the formation and growth of biominerals (55, 56).

Holobiont biometrics showed the strong regulation of algal symbiont density by light-mediated adjustments in skeletal features. These changes are achieved by phagocytosis-exocytosis-endocytosis with associated innate immune recognition (48). We identified associated sub-networks with enriched categories related to vesicle/vacuole-mediated transport (GO.0016192, 41 enriched genes, FDR < 0.001) (**Fig. 5C**, 78 nodes and 174 edges). The core sub-network of hub genes (**Fig. 5C)** interacted with spectrins, ankyrins, and key regulators of intracellular membrane traffic GTPases-RAB. Previous studies have emphasized pattern recognition receptors (PRR) as key players in symbiosis establishment (48). Main PPR identified are endocytosis mediator C-type lectin domain family member ($_{DMG\text{-}DEG}$*MRC1*) and Toll-like and Toll/interleukin-like receptors ($_{DEG}$*TLR6* and $_{DEG}$*TLR1*). Furthermore, we identified a sub-network associated to immune system responses (NEA, HSA-1280218, 18 enriched genes, FDR < 0.001) (**Fig. 5D**, 30 nodes and 195 edges), were hub genes ($_{DMG\text{-}DEG}$*POLA1*, $_{DMG}$*ATR*, $_{DMG}$*PIF1*, $_{DMG}$*FBXO18*) interacted with the strongly connected component through an E3 ubiquitin ligase that targets cell cycle regulatory proteins for degradation ($_{DMG}$*ANAPC1*). The targeted cluster was mainly transcriptional (both up- and down-regulated) and the few DMGs were also E3 ubiquitin ligases ($_{DMG\text{-}DEG}$*HECTD1*, $_{DMG}$*HERC1*, $_{DMG}$*HUWE1*).

Concluding remarks

Whole colony plasticity in the branching coral *A. palmata* resulted from the integration of modular responses to local variation in light availability. The plasticity of local modules was evident when fragments were transplanted to contrasting light environments, where significant changes in skeletal features prompted the optimization of light absorption and utilization to maximize metabolic outputs and growth. Recognizing this modular concept of plasticity is important in the face of heritability of colony-level traits versus local module-level traits. Animal colonies consisting of many modules may remain coherent entities where colony traits have the evolutionary potential to respond to natural selection (57). Remarkably, variants may arise locally, and single modules may have some evolutionary potential (58).

Local modular plasticity was accompanied by significant methylome and transcriptome modifications. Enhanced resolution with the MethyIT pipeline allowed us to examine meaningful associations between a natural phenotype, transcriptome and methylome modifications. Our data showed a significant light-mediated change in coral morphology, a phenotypic adjustment that was reflected in molecular signatures of changes in growth, including soft tissue growth and biomineralization. These observations suggest that symbiotic corals have acquired the capability of effecting an epigenomic response that incorporates whole methylome repatterning and is associated to changes in coral morphology. This interpretation aligns with previous whole genome

views that focused on the function of DNA methylation in phenotypic plasticity (59). The resolution allowed us to integrate genome-wide DNA methylation with gene expression datasets into meaningful biological networks. Our comprehensive network approach based on interactions from correlation matrix networks and gene interaction from curated databases for predicted networks offered a powerful approach to identify potential markers of plasticity in the interaction of DMGs and DEGs. Annotated genes *COL6A5, SPTAN1, PTK7, FGFR1, FBXO30, P4HA2, TNR, NID1, ITGAX, ANK3, RCHY1, GBF1,* and the transcription factor *SHOX*, were key regulators identified in sub-networks of hub genes in both analyses. These genes are involved in regulation of cell cycle, ECM, vesicular trafficking, immune regulation, regulation of transcription and transduction, and biomineralization. They represent candidates for further study.

Our analysis provides evidence of association of genic methylation repatterning with programmed changes in phenotype. One interpretation of these outcomes is that dramatic shifts in gene expression are accompanied by methylation changes that stabilize local chromatin to help reestablish homeostasis. However, environmental changes also induce non-random changes in gene body methylation that influence alternative splicing activity to modulate gene expression and phenotype (14, 60–62). While our data do not specifically provide information on regulation of gene expression, the integration of methylation and transcriptional information makes significant inroads in the identification of networks underpinning coral phenotypic plasticity and provides a roadmap for studies of other non-model organisms. As methylome repatterning is a signature of chromatin reorganization and 3D architecture, integrating datasets enhances the potential to identify essential interactions and likely signatures of gene-network coordination that may not be seen in DEG datasets alone (63). Our integrated analyses offered the potential to predict phenotype at the gene-network level and further postulate a light-mediated sequential response triggered by animal-sensing of initial light stimulus to the change in skeletal morphology (**Fig. 6**).

Materials and Methods

Light exposure conditions

We first characterized the natural light exposure within colonies of the coral *Acropora palmata* by measuring the incident light on both upperside and underside surfaces of *in situ* branches (base, mid-branch, tips). We estimated the vertical attenuation coefficient (K_d) of the water column and retrieved daily irradiance cycles from SAMMO light sensors (Meteorological and Oceanographic Monitoring Academic Service at UNAM). Light measurements were taken with a cosine-corrected quantum sensor (Diving-PAM, Walz, Germany) previously calibrated against a manufacturer-calibrated quantum sensor (LI-1400, LI-COR, USA). We identified two daily integrated PAR (Photosynthetically Active Radiation) conditions for *in situ* colonies that we also used for the experimental setup: High Light (HL) surfaces represent fragments from upperside surfaces of branches exposed to ~20 mol quanta m^2 day^{-1} and Low Light (LL) surfaces represent fragments exposed to ~2 mol quanta m^2 day^{-1} (4-10% of upperside exposure).

Coral sample collection and experimental setup

To induce phenotypic plasticity, we performed a reciprocal transplant experiment in the reef-lagoon (30 m from the reef crest) in Puerto Morelos Reef National Park, Mexican Caribbean (**Fig 2A**). We sampled 3 colonies (representing 3 distinct multilocus genotypes, or genets, as detected with Standard Tools for Acroporid Genotyping STAGdb (64)) from a depth of 2-3 m (permits No. SGPA/DGVS/06960/17 and No. SGPA/DGVS/07846/17), each at least 300 m apart. We collected ~7 cm^2 fragments from HL (n= 42) and LL (n = 42) surfaces of branch surfaces keeping track of genet identification. We settled them in a reef-deployed PVC structure designed to simulate the light condition and colony position of source colonies.

We placed all coral fragments in their original light condition and orientation (*i.e.* HL facing up) and allowed them to heal and acclimate for 8 weeks (when new growth was observed). Subsequently, we randomly divided HL fragments into control and treatment groups, equal grouping was done for LL fragments. To induce phenotypic plasticity, coral fragments in treatment groups were flipped to the opposite light condition and position (*i.e.* high light fragments were flipped to a low light condition, while LL fragments were flipped to a HL position) (**Fig. 2A**). This second acclimatory period was carried out for 5+ weeks. We estimated maximum excitation pressure over Photosystem II (Q_m=1 - [($\Delta F/F_m$' at noon) / (F_v/F_m at dusk)]) to determine successful acclimation to destination light condition (65). We further compared Q_m between experimental coral fragments (N=84) and *in situ* colonies (30 colonies, N=30 datapoints from upper and N=30 from underside surface of branches) (**Fig. S3A**).

Four group conditions were analyzed after 13+ weeks of experiment: HL controls (n= 21), HL→LL treatments (High Light to Low Light, n = 21) LL controls (n= 21), LL→HL treatments (Low Light to High Light, n = 21).

Phenotype data analysis

Structural traits

Phenotypic traits were measured based on parameters describing coral morphology and physiology after 13+ weeks of experiment (**Table 1**). (n = 12 per group condition for non-invasive techniques, and n=9 per group condition for invasive techniques such as host total protein content, chlorophyll *a* content, and symbiont cell counts) (**Fig. S1**). Morphological features were described by polyp density (number of polyps per area) and by corallite height (mm), defined as the vertical distance between the corallite base and the top of the theca. Corallite height was delineated into 'height classes' C_1 (0 - 1.5 mm), C_2 (>1.5 - 3 mm), and C_3 (>3 mm) to further estimate polyp density

at each height class. The projected area of each fragment was estimated with photography and used to normalize physiological and morphological parameters.

To describe the structural and optical properties of the tissue we measured reflectance (R) of the intact coral tissue as [De_{675} = log (1/R_{675})] and estimated absorbance at 675 nm (De_{675}) (66, 67). In addition, we estimated symbiont density, Chlorophyll (Chl) *a* and *c* from each fragment (66–68). Briefly, tissue extractions were carried out using an air gun and filtered sea water (FSW). Slurries obtained from this method were subsequently homogenized at low temperature (Tissue-Tearor Homogenizer BioSpec Inc, USA) and centrifuged. The resulting pellet was re-suspended in filtered seawater and preserved for symbiont cell counts (counted in a hemocytometer after the addition of 200 µl of iodine preservation solution), and for Chl concentration (extracted with acetone/dimethyl sulfoxide 95:5 vol/vol). Chl*a* and *c* concentrations (ρ pigment content per projected surface area in mg Chl m^{-2}) were estimated spectrophotometrically (3 reads per sample) with a modular spectrometer (Flame-T-UV-VIS, Ocean Optics Inc., USA) using the equations described by Jeffrey and Humphrey (69).

Downstream calculations of optical properties were performed integrating the parameters detailed above (35, 66). Symbiont density and Chl*a* were normalized to calculate Chl*a* per symbiont cell (Ci in pg Chl*a* sym^{-1}). The specific absorption coefficient of Chl*a* (a^*_{Chla}), a descriptor of the light absorption efficiency of the holobiont, was estimated as [$a^*_{Chla}=(De_{675}/\rho)\cdot\ln(10)$] (66). Other calculations included the specific absorption coefficient of symbionts *in hospite* (a^*_{sym}), a descriptor of the light absorption efficiency of symbionts. The host mass-specific efficiency (a^*_M), a descriptor of the light absorption efficiency per host mass, a descriptor that quantifies the potential benefits returned to the host, from the capacity of the symbiosis to collect solar energy.

Physiological traits

To estimate metabolic rates, we measured photosynthesis *in hospite* and estimated derived parameters. Photosynthetic responses (Photosynthesis - Quantum Energy curves, PE curves) of coral fragments were measured using a laboratory-made water-jacketed respirometer (70). Corals were incubated in filtered sea water at a constant temperature (28 °C) and constant water flow (generated by continuous agitation from magnetic stirrers). A Light Emitting Diode LED-system was designed to enable automation of light increments every 10 minutes. Oxygen evolution was measured continuously with a fiber-optic oxygen meter system (FireSting, Pyroscience) and the photosynthetic efficiency (α), compensation irradiance (E_c), saturation irradiance (E_k), respiration rates (R_d), and maximum photosynthetic rates (P_{max}), were calculated from the light-limited and light-saturated regions of the PE curves (68, 71). As a downstream calculation, the minimum quantum requirement of photosynthesis (Φ^{-1}_{O2}) was estimated based on the linear regression of photosynthetic rates during the light-limited region of PE curves. Φ^{-1}_{O2} is defined in terms of the light being absorbed and used to drive photosynthesis or photosynthetic utilizable radiation (PUR). The ratio of absorbed light is derived from previous measurements of reflectance [A = 1- R].

Similarities in phenotypic traits among the different group conditions and genets were analyzed with non-metric multidimensional scaling (NMDS) ordination, plotted via Bray-Curtis dissimilarity matrix and 9999 permutations in vegan R-package. Statistical support for the NMDS clustering is provided by the permutation-based hypothesis test analysis of similarities (ANOSIM) for experimental groups and for genets.

Coral tissue sampling and nucleic acid extraction

After 13+ weeks of experiment (**Table 1**), coral tissue from each fragment (n = 12 per group condition) was split into two samples and preserved, both in 95% ethanol and RNAlater (Ambion, Life Technology) and stored at -80 ºC until processing.

Genomic DNA (gDNA) was extracted from 32 *A. palmata* fragments (n= 8 per group condition; 16 fragments per genet). We used the DNeasy Blood and Tissue Kit (Qiagen, Switzerland), as per the manufacturer's protocol. gDNA concentration was quantified at 0.5-1.5 µg (Qubit® dsDNA BR

Assay Kit on a Qubit® 2.0. Fluorometer) and sent for Whole Genome Bisulfite Sequencing (WGBS) at Admera Health (New Jersey, USA).

Total RNA was extracted from the same 32 *A. palmata* fragments used in WGBS as previously noted. The tissue from each fragment was homogenized in TRIzol reagent (Ambion, Life Technology) before centrifugation with chloroform for 15 minutes at 12,000 x g at 4 ºC. The aqueous phase was then isolated and cleaned using Qiagen RNeasy Mini kit (Qiagen), as per the manufacturer's protocol with an additional on-column DNase treatment using RNase-Free DNase Set (Qiagen). To maximize concentration of eluted RNA, the same 35 µl of RNAse-free water was twice passed through the spin column for the final isolation step. Concentration and purity ($A_{260/280}$) were analyzed via NanoDrop ND-1000 spectrometer and quality assessed (RIN > 7) with Agilent 2100 Bioanalyzer (Agilent Technologies). Total RNA was sent to Admera Health (New Jersey, USA) where concentration and purity was re-analyzed (Qubit® dsDNA BR Assay Kit on a Qubit® 2.0. Fluorometer).

Methylome sequencing and data processing

Sequencing libraries were prepared with an average sequencing library insert size of 450 bp and according to TruSeq® DNA Methylation Kit protocol, Sample Preparation Guide (Illumina Inc., USA). Briefly, standard reaction mix consisting of 130 µl of the CT Conversion Reagent and 20 µl of each DNA sample were used for bisulfite conversion (EZ DNA Methylation-Gold™ Kit) in a thermal cycler (Eppendorf® Mastercycler® Pro S). After the incubation period, bisulfite converted DNA was purified following the protocol of EZ DNA Methylation-Gold™ Kit. The bisulfite converted sequencing library was enriched following the TruSeq® DNA Methylation Kit protocol. Libraries were validated and quantified with qPCR. Sequencing was performed in Illumina Hi-Seq platform with pair-end reads of 2x150 and a mean depth coverage of 30x (Illumina Inc., USA). The estimated number of passed filter reads per sample was 110-120 million paired-end reads (55-60M reads in each direction).

The expected bisulfate conversion efficiency for this method is >99%. While Lambda DNA was not spiked-in to estimate non-conversion and mis-sequencing rate, we can assume that only CpG methylation context occurs in corals (27, 72), hence, non-CpG methylation should be close to zero. We detected an average of 13.96% (SE=0.07) methylation in CpG context and an insignificant 0.54% (SE = 0.01) in non-CpG contexts (CHG and CHH, where H is A, T, or C), which resulted in an inferred bisulfite conversion efficiency of ~99.5%.

Data processing. Methylation analysis was performed using Bismark 020.0 (Krueger and Andrews, 2011). Briefly (**Fig. S2**), FASTQ files were quality-filtered, and adapter sequences trimmed using Trim Galore 0.5.0 (Krueger, 2018). A bisulfite-converted reference genome file was generated using Bismark-Bowtie2 algorithm, and the epigenome library sequenced data was aligned to the *Acropora palmata* genome (JAOVVL01). Methylation information was then extracted from the output SAM files and resulting genome tracks were used for the visualization and reporting of downstream differential methylation calculations. Methylated and unmethylated read counts for all cytosines across the genome in the CG, CHG, and CHH context were obtained from census files.

The approach used for downstream analysis was based on the identification of Differentially Methylated Positions (DMPs) and Differentially Methylated Genes (DMGs) using R package Methyl-IT 0.3.1.2 (19, 21, 41) (**Fig. S2**). Briefly, methylation count (COV) files were read into R to calculate Hellinger Divergence (*HD*, a variable used to measure methylation level divergence) by using the pool of methylation counts for control samples as reference. Potential DMPs (pDMPs) were estimated based on critical values of $HD_{\alpha=0.05}$ for each sample from the best fitted probability distribution model; in this case, a 3-parameter gamma distribution model. Final DMPs were estimated from the set of pDMPs by calculating the optimal cutoff threshold for *HD* based on Youden index. Generalized linear regression analysis (generalized linear model, GLM) was applied to test the difference between group DMP counts (among control and treatment groups; HL vs HL→LL, LL vs LL→HL) for selected genomic features. The fitting algorithm approaches provided

by glm and glm.nb functions from the R packages stat and MASS were used for Poisson (PR), Quasi-Poisson (QPR) and Negative Binomial (NBR) models with logarithmic link. The '*countTest2*' function in Methyl-IT was used to implement the selected model. The following parameters were applied to identify significant DMGs (41): 1) the minimum DMP count per bp on gene-body: *CountPerBp* = 2.5; 2) a minimum count per sample (on average) in at least 5 DMPs in one group: *minCountPerIndv* = 5; 3) a maximum coefficient of variance for each group: *maxGrpCV* = 1, 4) minimum value of the logarithm of fold-changes: *Minlog2FC* ≤ 1; 5) *p*-value cutoff: *pvalCutOff* = 0.01, 6) *p*-value adjustment was performed by Benjamini & Hochberg method: *pAdjustMethod* = "BH". Parameters 1 to 3 are addressed to prevent spurious DMGs, which cannot be rejected by the generalized linear regression algorithms.

Genes overcoming constraints 1 to 5 and displaying significant difference between control and treatment comparison according to likelihood ratio test (LRT) derived by the *anova* function from stats packages were identified as DMGs (**Fig. S2**). A detailed description of how to define and compute DMPs and potential DMGs is included in the Methyl-IT vignettes and the package manual, available at https://github.com/genomaths/MethylIT. *Acropora palmata* genome annotation file Apalm_assembly_v2.0_180910.gff3 was used to annotate genome features.

Methyl-IT downstream analysis (Methyl-IT.utils). A Hierarchical clustering (HC) was performed to provide an initial estimation of the number of possible groups and information on their members. The effectivity of HC depends on the experimental dataset, the metric used, and the glomeration algorithm applied. Ward's agglomeration algorithm was used as it performs much better on biological experimental datasets than the other of the available algorithms (e.g. UPGMA, UPGMC).

RNA sequencing and data processing

RNA libraries for 2x150bp paired-end sequencing were prepared using the NEBNext Ultra II Nondirectional Library Prep Kit with polyA selection (New England Biolabs, Inc.). Samples were run on one plate of the Illumina NovaSeq platform. Illumina universal adapters and reads below PHRED of 22 were trimmed using Cutadapt(73). Filtered reads were mapped to the *Acropora palmata* genome (JAOVVL01) using the RNA-seq aligner STAR (2.5.3a) with read count data generated by the –quantMode GeneCount parameter. Reads were verified using the generated BAM files for input into htseq-count.

Differential gene expression analysis. Gene count normalization and differential expression analysis was performed using DESeq2 3.12.0. Significant Differentially Expressed Genes (DEGs) were determined via pairwise comparison among control and treatment groups (HL vs HL⇒LL, LL vs LL⇒HL) and genet, with a false discovery rate-adjusted P value (FDR) of < 0.05 (**Fig. S2**).

Network-associated responses

A network provides a collection of nodes and edges that represent our system of elements (genes) interacting or regulating each other (42). Based on available data, we chose gene-gene interaction networks (predicted protein-protein interaction networks), as they are undirected, and the graph is non-sequential (X affects Y, but we do not know how) (74). A key feature for the biological interpretation of graph properties are hubs. Small-degree nodes (with small number of interactions) are the most abundant, but high-degree nodes or hubs, although less frequent, have a much higher number of interactions (75). In this context, the likelihood that a gene is essential correlates with the number of interactions, and random node disruption will not lead to major losses of connectivity. In contrast, the loss of hubs will cause a major breakdown of the network (42, 76, 77).

Agnostic biological network analysis: Network-based integration of DMG and DEG datasets (**Fig. S2**)**.**

To understand the interaction between the change in methylomes (n = 32) and transcriptomes (n = 32), and how genes contributed to the change in phenotype, we performed a Weighted Gene Correlation Network Analysis (WGCNA 1.71) (43). We generated a dataset (gene list) comprising the subsets of 1) all DMGs (from Methyl-IT 0.3.1.2) and 2) DEGs (from DESeq2 3.12.0) that presented at least one DMP (from Methyl-IT 0.3.1.2) after the change in light treatment. This dataset included outputs from all groups (HL, HL→LL, LL, LL→HL) and genets to discover general patterns of gene contribution. Additionally, a binary annotation was included to keep track of DMG, DEG and both DMG-DEG. As a results, each sample was represented as vector of 3272 genes/coordinates, where each coordinate was given by the sum of *HD* at each DMP on the given gene.

We first performed a hierarchical clustering (HC) applying Ward's agglomeration algorithm to provide an initial estimation of the number of possible groups and information on their members. Methyl-IT function *pcaLDA* was used to perform a Principal Component Analysis (PCA) and a PCA + Linear Discriminant Analysis (LDA). Unlike hierarchical clustering (HC) and PCA, LDA is a supervised machine learning approach, therefore, we must provide a prior classification of the samples, which can be derived, for example, from the HC, or from a previous exploratory analysis with PCA. Based on the cumulative proportion of variance, the PC1 and PC2 carried 92% of the total sample variance and could split the samples into meaningful groups. We saved the loadings from each gene. Loadings are coefficients in linear combination predicting a variable by the (standardized) components. The sum of loading squares within each component are the eigenvalues (components' variances), which is 1 for standardized loadings. In other words, loadings are "standard deviations" and the square of the loading of gene "A" quantitatively expresses the percent of the PC variance carried by gene "A". PC-scores for each gene indicate the discriminatory power in the clustering (control vs treatment) and its genomic/epigenomic contribution (in terms of proportion of the whole phenotypic variance) to the change in phenotype.

Genes PC-scores (gene-score) from 14 PCs were then used to build the pairwise correlation matrix for the WGCNA. Kendal's tau correlation was selected since it is better at detecting nonlinear behaviors and is more conservative than Pearson's correlation. The resulting weighted correlation matrix was then constructed as a network in the R-package WGCNA (43) and exported as edge list (interactions with weights) and node list files with assigned modules into Cytoscape 3.8.2 for visualization. Each entity of the dataset is a (gene) node, and 2 nodes are connected if their correlation or distance reach a threshold (here set to 0.4). Network topology included gene discriminatory power (gene-scores) and a measure of how similarly they contributed to this classification (weight from correlation). The correlation network was analyzed and visualized in Cytoscape 3.8.2 (19).

Predicted biological networks: network-associated responses from DMGs (**Fig. S2**)**.** To identify the biological meaning of potential relationships among DMGs we inferred gene interaction networks from *stringApp* in Cytoscape 3.8.2. The associations in the *string* database provides known and predicted protein−protein associations data for many organisms, including both physical interactions and functional associations, by integrating available experimental data and pathways from curated databases (44, 45). We used only our detected DMGs (without network expansion) as input in *string protein query* (Swiss-Prot hit name) to retrieve an arbitrary long list of nodes and interactions. This approach is generally used to retrieve string networks from proteomics and transcriptomics studies (44, 45) .

The best hit for baseline networks was reached with *string query* for *Homo sapiens*. We recognize that cross-species knowledge transfer is quite challenging because the phylum cnidaria diverged from Bilateria 550 million years ago and may have fundamentally different genetic architectures. Also, as species diverge, protein functions change and are re-purposed through divergent and convergent evolution, and genetic interactions are often rewired (78). Parallel to this, in network-based approaches most predicted interactions for each species are not experimentally verified. Despite these limitations, the best hit in *string query* was still *Homo sapiens*, perhaps, due to the presence of conserved stress response, conserved pathways (*e.g.* extrinsic and intrinsic

apoptotic pathways, ion trafficking system) and (predicted) gene products between early and late branching metazoans at the molecular level (48, 53, 79–81). Furthermore, genes that emerged from our data and clustering analyses predicted gene interactions associated to coral biological processes that aligned well to the measured phenotypes, suggesting our analytical approach was plausible.

The retrieved baseline network was then analysed statistically incorporating extended centrality measures from CentiScape 2.2 App (EigenVector of centrality). We chose Eigenvector centrality because this attribute ranks nodes by taking into consideration not only the number of interactions of a node (degree), but also, the centrality of the interactions that it is connected to. In other words, a node is important if it is interacting with other important nodes. The output dataset generated from Methyl-IT 0.3.1.2 was imported into this network to assign node attributes.

To identify hub genes, we assigned methylation signal and Eigenvector of centrality as attributes to the nodes (19). In networks, a protein with a very high Eigenvector is a protein interacting with several important proteins (regulating them or being regulated by them), thus suggesting a central super-regulatory role or a critical target of a regulatory pathway. We used Eigenvector as parameter to perform k-means clustering algorithm (*clusterMakerApp* in Cytoscape 3.8.2.) (19) to identify clusters of hub genes. To identify over-represented functions in the large set of DMGs, we performed Network Enrichment Analysis (NEA). Enriched terms were retrieved as UniProt KnowledgeBase (kw) categories in String Enrichment App in Cytoscape 3.8.2 (19).

Predicted biological networks: Network-associated responses from DEGs. To identify the biological meaning of potential relationships among DEGs we inferred gene interaction networks from *stringApp* in Cytoscape 3.8.2 with the same workflow as for DMGs interaction networks. The output dataset generated in DESeq2 3.12.0 was imported to this baseline network to assign gene regulation (up-regulated or down-regulated) as a node attribute.

Predicted biological networks: Network-based integration of DMG and DEG datasets.

To further explore the association between DMGs and DEGs, we integrated DEGs to DMGs network data sets. The integration was done at the cluster level (after *clusterMakerApp* independent analyses) with the criteria that a DEG-cluster be selected if it contained at least one gene also identified as DMG. The output datasets generated from Methyl-IT 0.3.1.2 and DESeq2 3.12.0 were imported to this baseline network to assign node attributes. With this approach we were able to enhance networks by adding new attributes to the nodes: DMG, DEG, both DMG-DEG. We maintained the attributes Eigenvector of centrality, methylation signal (from Methyl-IT 0.3.1.2), and gene regulation (upregulated or downregulated from DESeq2 3.12.0). A new clustering was performed based of Eigenvector of centrality ranks and 1st, 2nd and 3rd neighbours of high ranked nodes. To identify over-represented functions in the DMGs-DEGs integrated clusters, we performed a Network Enrichment Analysis (NEA) to each new cluster. Enriched terms were retrieved as UniProt KnowledgeBase categories (kw) in String Enrichment App (19). Because key coral biological processes emerged from the new clustering, we further explored potential key regulators and candidate genes involved in light-mediated phenotypic plasticity of structural traits in corals.

Acknowledgments

We thank UNAM and ICMyL for staff support, facility assistance, SAMMO data. PASPA-DGAPA to S.E. for sabbatical at PSU-Biology. M.K. Durante for assistance in laboratory and computational work. Collection permits No. SGPA/DGVS/06960/17 and No. SGPA/DGVS/07846/17 to SE, CITES permit MX90225 to SE. **Funding:** This project has received funding from The Pennsylvania State University SEED Grant program awarded to I.B.B., R.I.P. and S.A.M; from NSF grant (NSF OCE-1537959) to I.B.B., NIH grant (NIH R01 GM134056-01) to S.A.M., and The Pennsylvania State University Start-up to R.I.P. **Ethics declarations**: This article does not contain any studies with human participants or animals where formal consent is required, and ethics approval for this study

was not required. **Data and materials availability:** All data are available in the main text or the Supplementary Information Appendix. The datasets generated during the current study will be available (in Dryad) at the time of publication. All sequencing data will be deposited in the National Center for Biotechnology Information (NCBI) at the time of publication. Custom codes used for methylation analysis with Methyl-IT are available at https://genomaths.github.io/.

References

1. A. B. Nicotra, *et al.*, Plant phenotypic plasticity in a changing climate. *Trends Plant Sci* **15**, 684–692 (2010).
2. L. M. Chevin, R. Lande, G. M. Mace, Adaptation, plasticity, and extinction in a changing environment: Towards a predictive theory. *PLoS Biol* **8**, e1000357 (2010).
3. G. Torda, *et al.*, Rapid adaptive responses to climate change in corals. *Nat Clim Chang* **7**, 627–636 (2017).
4. R. Borges, Plasticity comparisons between plants and animals. *Plant Signal Behav* **3**, 367–375 (2008).
5. R. K. Trench, Microalgal-Invertebrate symbioses : a Review. *Endocytobiosis Cell Res* **9**, 135–175 (1993).
6. J. P. Gattuso, D. Allemand, M. Frankignoulle, Photosynthesis and calcification at cellular, organismal and community levels in coral reefs: A review on interactions and control by carbonate chemistry. *Am Zool* **39**, 160–183 (1999).
7. T. C. LaJeunesse, *et al.*, Systematic Revision of Symbiodiniaceae Highlights the Antiquity and Diversity of Coral Endosymbionts. *Current Biology* **28**, 2570-2580.e6 (2018).
8. P. G. Falkowski, Z. Dubinsky, L. Muscatine, J. W. Porter, Light and the Bioenergetics of a Symbiotic Coral. *Bioscience* **34**, 705–709 (1984).
9. S. Enríquez, E. R. Méndez, O. Hoegh-Guldberg, R. Iglesias-Prieto, Key functional role of the optical properties of coral skeletons in coral ecology and evolution. *Proceedings of the Royal Society B: Biological Sciences* **284**, 20161667 (2017).
10. A. Malik, *et al.*, Molecular and skeletal fingerprints of scleractinian coral biomineralization: From the sea surface to mesophotic depths. *Acta Biomater* **120**, 263–276 (2021).
11. D. Buitrago, *et al.*, Impact of DNA methylation on 3D genome structure. *Nat Commun* **12** (2021).
12. T. Hashimshony, J. Zhang, I. Keshet, M. Bustin, H. Cedar, “The role of DNA methylation in setting up chromatin structure during development” (2003).
13. O. Bossdorf, D. Arcuri, C. L. Richards, M. Pigliucci, Experimental alteration of DNA methylation affects the phenotypic plasticity of ecologically relevant traits in Arabidopsis thaliana. *Evol Ecol* **24**, 541–553 (2010).
14. G. Lev Maor, A. Yearim, G. Ast, The alternative role of DNA methylation in splicing regulation. *Trends in Genetics* **31** (2015).
15. K. J. F. Verhoeven, J. J. Jansen, P. J. van Dijk, A. Biere, Stress-induced DNA methylation changes and their heritability in asexual dandelions. *New Phytologist* **185**, 1108–1118 (2010).
16. K. J. F. Verhoeven, B. M. VonHoldt, V. L. Sork, Epigenetics in ecology and evolution: What we know and what we need to know. *Mol Ecol* **25**, 1631–1638 (2016).
17. X. Yang, S. A. Mackenzie, “Approaches to Whole-Genome Methylome Analysis in Plants” in *Methods in Molecular Biology*, (Humana Press Inc., 2020), pp. 15–31.
18. H. Kundariya, R. Sanchez, X. Yang, A. Hafner, S. A. Mackenzie, Methylome decoding of RdDM-mediated reprogramming effects in the Arabidopsis MSH1 system. *Genome Biol* **23** (2022).
19. R. Sanchez, S. A. Mackenzie, Integrative Network Analysis of Differentially Methylated and Expressed Genes for Biomarker Identification in Leukemia. *Sci Rep* **10**, 1–16 (2020).
20. R. Sanchez, S. A. Mackenzie, Genome-wide discriminatory information patterns of cytosine DNA methylation. *Int J Mol Sci* **17**, 938 (2016).
21. R. Sanchez, X. Yang, T. Maher, S. A. Mackenzie, Discrimination of DNA methylation signal from background variation for clinical diagnostics. *Int J Mol Sci* **20**, 5343 (2019).

22. A. Hafner, S. Mackenzie, Re-analysis of publicly available methylomes using signal detection yields new information. *Sci Rep* **13**, 3307 (2023).
23. G. Dixon, Y. Liao, L. K. Bay, M. V. Matz, Role of gene body methylation in acclimatization and adaptation in a basal metazoan. *Proc Natl Acad Sci U S A* **115**, 13342–13346 (2018).
24. M. K. Durante, I. B. Baums, D. E. Williams, S. Vohsen, D. W. Kemp, What drives phenotypic divergence among coral clonemates of Acropora palmata? *Mol Ecol* **28**, 3208–3224 (2019).
25. J. A. Rodríguez-Casariego, *et al.*, Genome-Wide DNA Methylation Analysis Reveals a Conserved Epigenetic Response to Seasonal Environmental Variation in the Staghorn Coral Acropora cervicornis. *Front Mar Sci* **7**, 822 (2020).
26. H. M. Putnam, J. M. Davidson, R. D. Gates, Ocean acidification influences host DNA methylation and phenotypic plasticity in environmentally susceptible corals. *Evol Appl* **9**, 1165–1178 (2016).
27. Y. J. Liew, *et al.*, Epigenome-associated phenotypic acclimatization to ocean acidification in a reef-building coral. *Sci Adv* **4**, eaar8028 (2018).
28. J. L. Dimond, S. B. Roberts, Germline DNA methylation in reef corals: Patterns and potential roles in response to environmental change. *Mol Ecol* **25**, 1895–1904 (2016).
29. J. L. Dimond, S. K. Gamblewood, S. B. Roberts, Genetic and epigenetic insight into morphospecies in a reef coral. *Mol Ecol* **26**, 5031–5042 (2017).
30. S. B. Roberts, M. R. Gavery, Is there a relationship between DNA methylation and phenotypic plasticity in invertebrates? *Front Physiol* **2 JAN**, 116 (2012).
31. R. Sanchez, S. A. Mackenzie, Information thermodynamics of cytosine DNA methylation. *PLoS One* **11** (2016).
32. Y. X. Ow, P. A. Todd, Light-induced morphological plasticity in the scleractinian coral Goniastrea pectinata and its functional significance. *Coral Reefs* **29**, 797–808 (2010).
33. S. Enríquez, E. R. Méndez, R. Iglesias-Prieto, Multiple scattering on coral skeletons enhances light absorption by symbiotic algae. *Limnol Oceanogr* **50**, 1025–1032 (2005).
34. P. G. Falkowski, Z. Dubinsky, K. Wyman, Growth-irradiance relationships in phytoplankton. *Limnol Oceanogr* **30**, 311–321 (1985).
35. T. Scheufen, W. E. Krämer, R. Iglesias-Prieto, S. Enríquez, Seasonal variation modulates coral sensibility to heat-stress and explains annual changes in coral productivity. *Sci Rep* **7**, 4937 (2017).
36. I. B. Baums, M. K. Devlin-Durante, T. C. LaJeunesse, New insights into the dynamics between reef corals and their associated dinoflagellate endosymbionts from population genetic studies. *Mol Ecol* **23**, 4203–4215 (2014).
37. D. W. Kemp, *et al.*, Spatially distinct and regionally endemic Symbiodinium assemblages in the threatened Caribbean reef-building coral Orbicella faveolata. *Coral Reefs* **34**, 535–547 (2015).
38. I. B. Baums, M. W. Miller, M. E. Hellberg, Geographic variation in clonal structure in a reef-building Caribbean coral, Acropora palmata. *Ecol Monogr* **76**, 503–519 (2006).
39. H. De Kroon, H. Huber, J. F. Stuefer, J. M. Van Groenendael, A modular concept of phenotypic plasticity in plants. *New Phytologist* **166**, 73–82 (2005).
40. M. Pelizzola, J. R. Ecker, The DNA methylome. *FEBS Lett* **585**, 1994–2000 (2011).
41. X. Yang, *et al.*, Segregation of an MSH1 RNAi transgene produces heritable non-genetic memory in association with methylome reprogramming. *Nat Commun* **11** (2020).
42. R. Albert, Scale-free networks in cell biology. *J Cell Sci* **118**, 4947–4957 (2005).
43. P. Langfelder, S. Horvath, WGCNA: An R package for weighted correlation network analysis. *BMC Bioinformatics* **9** (2008).
44. D. Szklarczyk, *et al.*, The STRING database in 2017: Quality-controlled protein-protein association networks, made broadly accessible. *Nucleic Acids Res* **45**, D362–D368 (2017).
45. N. T. Doncheva, J. H. Morris, J. Gorodkin, L. J. Jensen, Cytoscape StringApp: Network Analysis and Visualization of Proteomics Data. *J Proteome Res* **18**, 623–632 (2019).
46. J. Stadler, H. Richly, Regulation of DNA repair mechanisms: How the chromatin environment regulates the DNA damage response. *Int J Mol Sci* **18** (2017).

47. N. Huck-Hui, A. Bird, DNA methylation and chromatin modification. *Curr Opin Genet Dev* **9**, 158–163 (1999).
48. S. K. Davy, D. Allemand, V. M. Weis, Cell Biology of Cnidarian-Dinoflagellate Symbiosis. *Microbiology and Molecular Biology Reviews* **76**, 229–261 (2012).
49. I. Cohen, Z. Dubinsky, J. Erez, Light enhanced calcification in hermatypic corals: New insights from light spectral responses. *Front Mar Sci* **2** (2016).
50. I. Taubner, M. Y. Hu, A. Eisenhauer, M. Bleich, Electrophysiological evidence for light-activated cation transport in calcifying corals. *Proceedings of the Royal Society B: Biological Sciences* **286** (2019).
51. Z. Kozmik, *et al.*, Assembly of the cnidarian camera-type eye from vertebrate-like components. *Proc Natl Acad Sci U S A* **105**, 8989–8993 (2008).
52. E. M. Hemond, S. T. Kaluziak, S. V. Vollmer, The genetics of colony form and function in Caribbean Acropora corals. *BMC Genomics* **15** (2014).
53. J. L. Drake, *et al.*, Proteomic analysis of skeletal organic matrix from the stony coral Stylophora pistillata. *Proc Natl Acad Sci U S A* **110**, 3788–3793 (2013).
54. E. Gutner-Hoch, H. W. Ben-Asher, R. Yam, A. Shemesh, O. Levy, Identifying genes and regulatory pathways associated with the scleractinian coral calcification process. *PeerJ* **2017**, 3590 (2017).
55. M. P. Mummadisetti, J. L. Drake, P. G. Falkowski, The spatial network of skeletal proteins in a stony coral. *J R Soc Interface* **18** (2021).
56. D. Allemand, É. Tambutté, J. P. Girard, J. Jaubert, Organic matrix synthesis in the scleractinian coral Stylophora pistillata: Role in biomineralization and potential target of the organotin tributyltin. *Journal of Experimental Biology* **201**, 2001–2009 (1998).
57. C. Simpson, A. Herrera-Cubilla, J. B. C. Jackson, How colonial animals evolve. *Sci Adv* **6**, 1–9 (2020).
58. K. L. Vasquez Kuntz, *et al.*, Inheritance of somatic mutations by animal offspring. *Sci Adv* **8**, 31 (2022).
59. Y. J. Liew, *et al.*, Epigenome-associated phenotypic acclimatization to ocean acidification in a reef-building coral. *Sci Adv* **4**, eaar8028 (2018).
60. J. Zhang, Y. Z. Zhang, J. Jiang, C. G. Duan, The Crosstalk Between Epigenetic Mechanisms and Alternative RNA Processing Regulation. *Front Genet* **11** (2020).
61. X. Yang, *et al.*, Gene body methylation can alter gene expression and is a therapeutic target in cancer. *Cancer Cell* **26**, 577–590 (2014).
62. I. Ausin, M. V. C. Greenberg, C. F. Li, S. E. Jacobsen, The splicing factor SR45 affects the RNA-directed DNA methylation pathway in Arabidopsis. *Epigenetics* **7**, 29–33 (2012).
63. W. Ouyang, Z. Cao, D. Xiong, G. Li, X. Li, Decoding the plant genome: From epigenome to 3D organization. *Journal of Genetics and Genomics* **47**, 425–435 (2020).
64. S. A. Kitchen, *et al.*, STAGdb: a 30K SNP genotyping array and Science Gateway for Acropora corals and their dinoflagellate symbionts. *Sci Rep* **10**, 1–18 (2020).
65. R. Iglesias-Prieto, V. H. Beltrán, T. C. LaJeunesse, H. Reyes-Bonilla, P. E. Thomé, Different algal symbionts explain the vertical distribution of dominant reef corals in the eastern Pacific. *Proceedings of the Royal Society B: Biological Sciences* **271**, 1757–1763 (2004).
66. S. Enríquez, E. R. Méndez, R. Iglesias-Prieto, Multiple scattering on coral skeletons enhances light absorption by symbiotic algae. *Limnol Oceanogr* **50**, 1025–1032 (2005).
67. R. M. Vásquez-Elizondo, *et al.*, Absorptance determinations on multicellular tissues. *Photosynth Res* **132**, 311–324 (2017).
68. Iglesias-Prieto R., R. K. Trench, Acclimation and adaptation to irradiance in symbiotic dinoflagellates. 1.Responses of the photosynthetic unit to changes in photon flux density. *Mar Ecol Prog Ser* **113**, 163–176 (1994).
69. S. W. Jeffrey, G. F. Humphrey, New spectrophotometric equations for determining chlorophylls a, b, c1 and c2 in higher plants, algae and natural phytoplankton. *Biochemie und Physiologie der Pflanzen* **167**, 191–194 (1975).
70. A. Rodríguez-Román, X. Hernández-Pech, P. E. Thomé, S. Enríquez, R. Iglesias-Prieto, Photosynthesis and light utilization in the Caribbean coral Montastraea faveolata recovering from a bleaching event. *Limnol Oceanogr* **51**, 2702–2710 (2006).

71. R. Osinga, R. Iglesias-Prieto, S. Enriquez, Measuring Photosynthesis in Symbiotic Invertebrates: A Review of Methodologies, Rates and Processes. *Applied Photosynthesis* (2012) https:/doi.org/10.5772/29339.
72. S. A. Trigg, *et al.*, Invertebrate methylomes provide insight into mechanisms of environmental tolerance and reveal methodological biases. *Mol Ecol Resour* **22**, 1247–1261 (2022).
73. M. Martin, Cutadapt removes adapter sequences from high-throughput sequencing reads. *EMBnet J* **17**, 10 (2011).
74. N. Le Novere, Quantitative and logic modelling of molecular and gene networks. *Nat Rev Genet* **16**, 146–158 (2015).
75. W. C. Dennison, R. S. Alberte, Photosynthetic Responses of Zostera marina L. (Eelgrass) to in situ Manipulations of Light Intensity. *Oecologia* **55**, 137–144 (1982).
76. H. Jeong, S. P. Mason, A. L. Barabási, Z. N. Oltvai, Lethality and centrality in protein networks. *Nature* **411**, 41–42 (2001).
77. M. R. Said, T. J. Begley, A. V. Oppenheim, D. A. Lauffenburger, L. D. Samson, Global network analysis of phenotypic effects: Protein networks and toxicity modulation in Saccharomyces cerevisiae. *Proc Natl Acad Sci U S A* **101**, 18006–18011 (2004).
78. J. Fan, *et al.*, Functional protein representations from biological networks enable diverse cross-species inference. *Nucleic Acids Res* **47**, 1–13 (2019).
79. D. Bhattacharya, *et al.*, Comparative genomics explains the evolutionary success of reef-forming corals. *Elife* **5**, 1–26 (2016).
80. L. Courtial, *et al.*, The c-Jun N-Terminal kinase prevents oxidative stress induced by UV and thermal stresses in corals and human cells. *Sci Rep* **7**, 1–10 (2017).
81. A. Ottaviani, *et al.*, Longevity strategies in response to light in the reef coral Stylophora pistillata. *Sci Rep* **10**, 1–10 (2020).

Figures and Tables

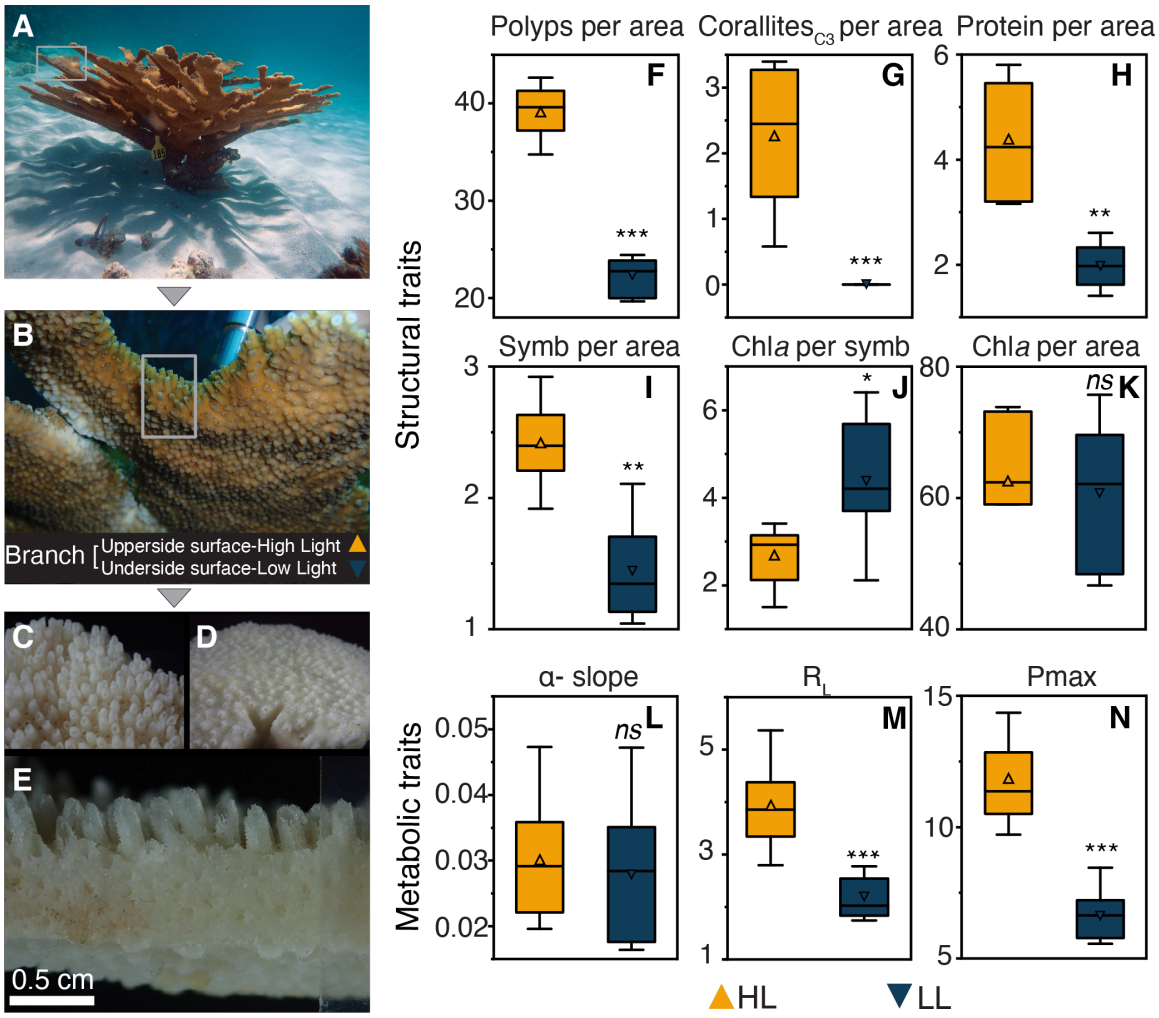

Figure 1. Phenotypic plasticity of *Acropora palmata* in response to light availability. (A) *A. palmata* colonies have a strong intracolonial light gradient. The branching morphology exhibits modules (polyps) exposed to direct sunlight (HL surfaces) and modules growing in the shade (LL surfaces). (**B**) Morphological skeletal features of the branch cross-section showing the transition from upperside to underside of the branch. (**C**) HL surfaces and (**D**) LL surfaces show distinct skeletal morphology, (**E**) with corallites significantly taller in the surface exposed to HL. (**F-N**) Phenotypic traits of HL (n= 21) and LL surfaces (n=21) from 3 genets. Center lines show the median and center squares the mean; box limits indicate the 25th and 75th percentiles; whiskers extend 1 time the interquartile range. For all panels, ***P <0.001; **P <0.01; *P<0.05; ^{ns}P >0.05, two-tailed, unpaired Student's t test. (**F**) Polyp density (# polyps cm^{-2}), (**G**) Density of corallites larger than 3 mm in height (# polyps cm^{-2}), (**H**) soluble host protein (mg protein cm^{-2}), (**I**) symbiont density (# sym cm^{-2}), (**J**) Chl*a* per symbiont cell (Ci, pg Chl*a* sym^{-1}), (**K**) Chl*a* density (mg Chl*a* m^{-2}), (**L**) photosynthetic efficiency (µmol O_2 µmol quanta), (**M**) respiration rate (µmol O_2 m^{-2} s^{-1}), (**N**) maximum photosynthetic rate (µmol O_2 m^{-2} s^{-1}).

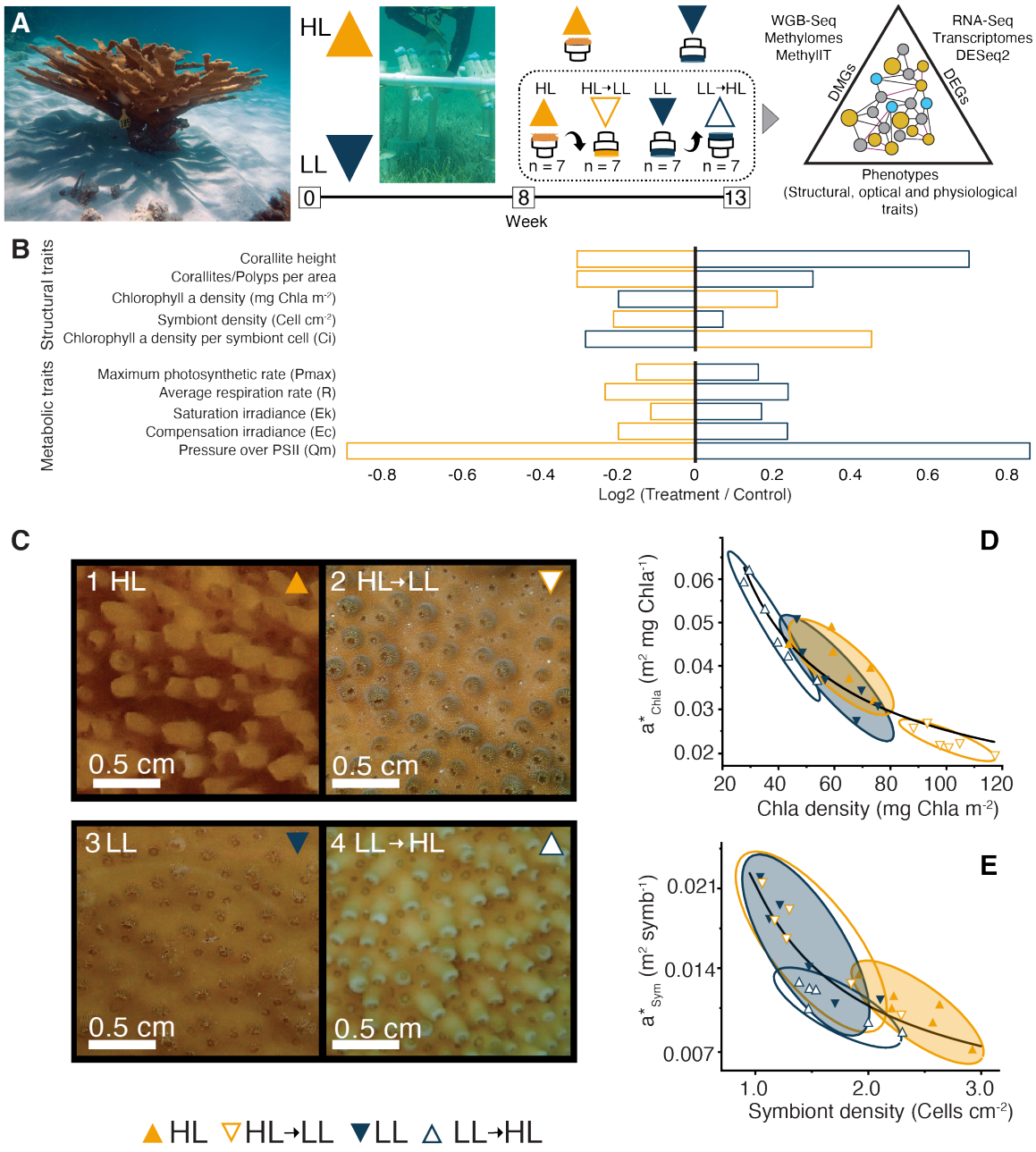

Figure 2. Induced phenotypic plasticity with reciprocal transplants. (**A**) Schematic representation of the experimental design. Control fragments from HL (n=7 per genet) and LL (n=7 per genet) remained unchanged, while treatment fragments (HL→LL, n=7 per genet; LL→HL, n=7 per genet) were manipulated in a reciprocal transplant that altered their light exposure by ~80%. After 13 weeks, light phenotypes were described, and tissue was collected for genomic and epigenomic analyses. (**B**) Fold change of main phenotypic traits showing the acclimatory mechanism to the destination light condition. (**C**) Visual inspection of one genet after 5+ weeks showing the change in corallite height and density. (**D-E**) Changes in optical traits based on specific absorption coefficients, a^*_{Chla} which describes the holobiont's efficiency to absorb light and a^*_{sym} , which describes *in hospite* light absorption efficiency of the algal symbionts.

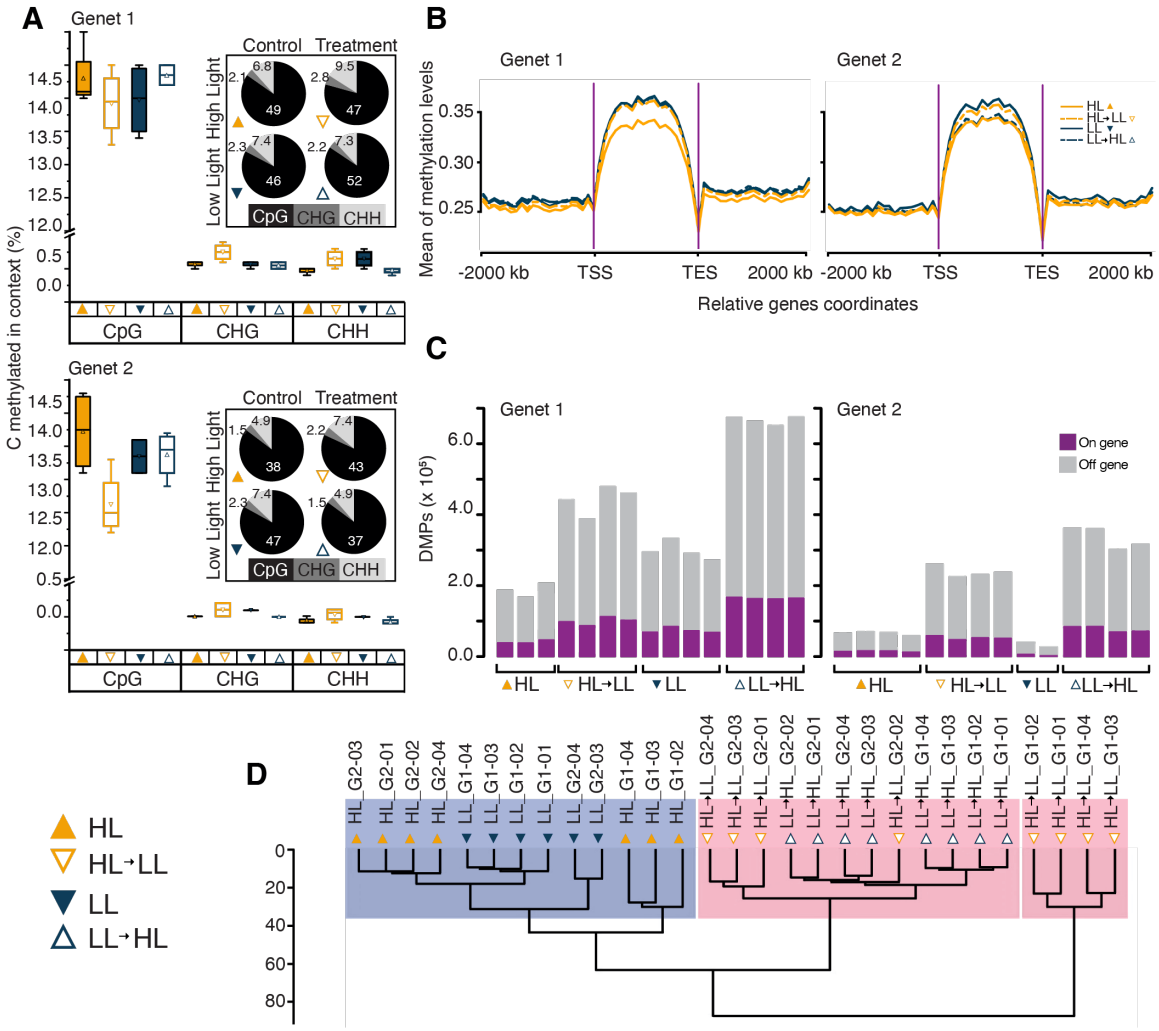

Figure 3. DNA Methylation context and light-mediated methylome repatterning. (**A**) Proportion of methylated cytosines (n = 8 per group condition) where highest in the CpG context and insignificant in CHG, and CHH contexts. Pie charts show the number of Cytosines (x 10^6) in each context. (**B**) Mean methylation levels of all cytosines were highest at genic regions; 2kb upstream of Transcription Start Site (TSS), and 2kb downstream of Transcription End Site (TES) are shown. Methylation levels were computed, divided to 60 bins, and plotted by genet and group condition. (**C**) Number of DMPs per group conditions identified by Methyl-IT, with centroid of control groups used as reference. DMPs were always higher in treatments than control samples. Two *A. palmata* genets are shown for comparison. (**D**) Hierarchical clustering of DMPs in genic regions classified by Hellinger Divergence. Classification of samples separated control (purple) and treatment (red) samples regardless of genet or destination light treatment.

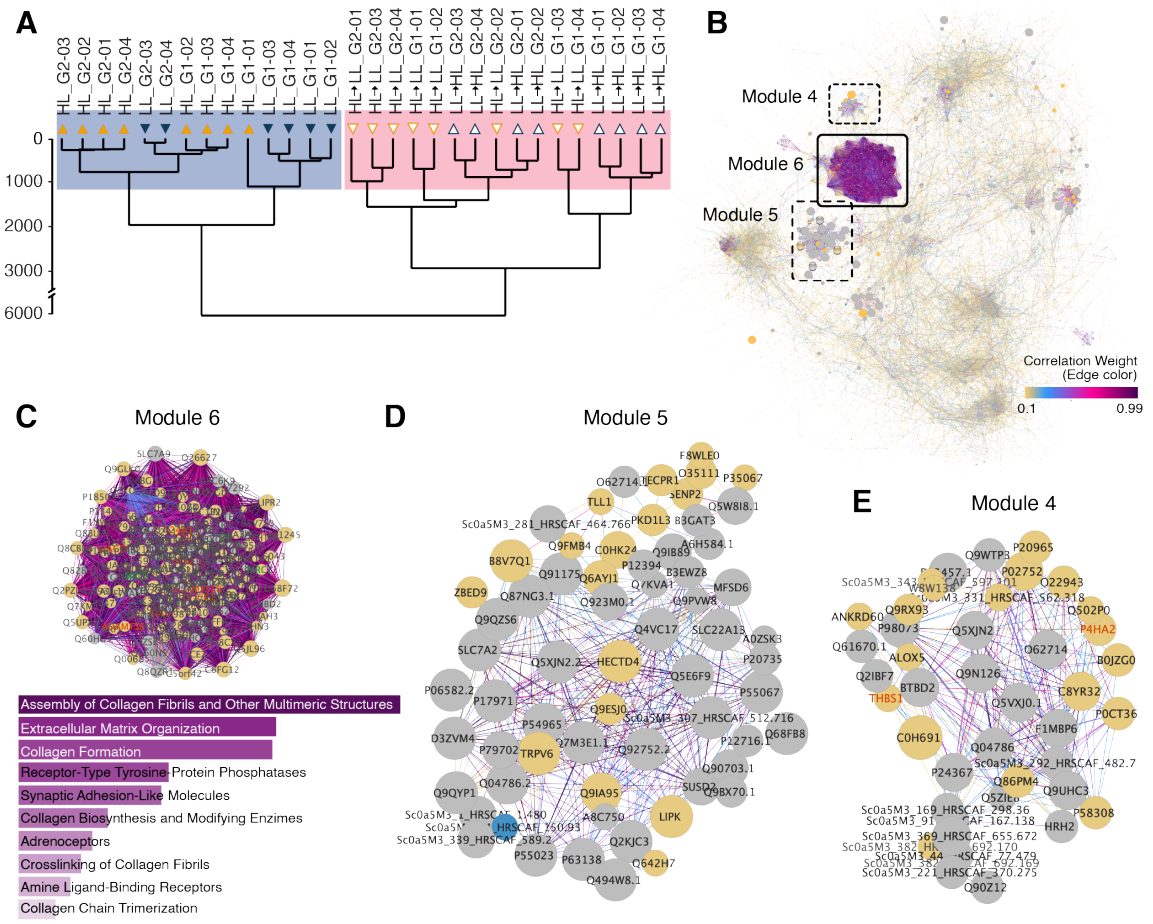

F

#	Display	Name	Gene-score
1	Q68F72	DMG SLC15A4	0.340
2	Q26627	DMG REJ	0.328
3	Q5JL96	DMG LOC4324695	0.328
4	GLIPR2	DMG GLIPR2	0.323
5	SLC7A9	DEG SLC7A9	0.319
6	P41245	DMG MMP9	0.318
7	C6FG12	DMG NLRC5	0.313
8	Q9GLK0	DMG TGM1	0.303
9	Q2PZL6	DMG FAT4	0.302
10	P18503	DMG P18503	0.300

G

#	Display	Name	Gene-score
1	SLC7A2	DEG SLC7A2	0.999
2	Q5E6F9	DEG PANP	0.999
3	Q5XJN2.2	DEG IFI30	0.999
4	D3ZVM4.2	DEG TRIM71	0.999
5	P55023	DEG MELC2	0.999
6	Q4VC17.1	DEG ADAMTS18	0.999
7	Q7M3E1.1	DEG CTRC	0.999
8	HECTD4	DMG HECTD4	0.999
9	Q04786.2	DEG HEX	0.992
10	Q2KJC3	DEG MPEG1	0.991

Cont... ▶

#	Display	Name	Gene-score
▶11	P55067	DEG NCAN	0.989
12	Q68FB8	DEG DEGS1	0.982
13	SLC22A13	DEG SLC22A13	0.972
14	P17971.1	DEG SHAL	0.971
15	Q9QYP1.1	DEG LRP4	0.968
16	P63138	DEG GABRB2	0.965
17	Q87NG3.1	DEG VP1905	0.942
18	Q91175	DEG ADRA1AA	0.940
19	Q92752.2	DEG TNR	0.939
20	Q494W8.1	DEG CHRFAM7A	0.932

H

#	Display	Name	Gene-score
1	C0H691	DMG LOC114955386	0.918
2	BTBD2	DEG BTBD2	0.871
3	O62714	DEG CASR	0.856
4	C8YR32	DMG LOXHD1	0.843
5	Q5VXJ0.1	DEG LIPK	0.842
6	F1MBP6.1	DEG KLHL3	0.842
7	Q5XJN2	DEG IFI30	0.842
8	Q9N126.2	DEG RDH8	0.842
9	Q04786	DEG HEX	0.842
10	Q9UHC3.1	DEG ASIC3	0.834

Figure 4. Methylomes-transcriptomes-derived agnostic network, analysis with WGCNA. The data was prepared by combining DMG and DEG datasets to one large dataset. To estimate the initial number of possible groups we performed a (**A**) hierarchical clustering (Ward's agglomeration algorithm), which showed a classification of samples separating controls (purple) and treatments (red) groups regardless of genet or destination light treatment. PCA (PC1 and PC2 carried 92% of the total sample variance) and a linear discriminant analysis (**Fig. S7**) were further performed to assign gene discriminatory power from PC-scores (gene-score) and build the pairwise correlation matrix (Kendal's tau correlation). The network was constructed in WGCNA 1.71, with module visualization and statistical analysis in Cytoscape 3.8.2. (**B**) Whole network of gene-gene interactions. (**C**) Type I subnetwork showing genes with strongest gene-gene interactions (edges with strongest weights from correlation but low gene-score), denotating genes that have similar contribution to the change in phenotype (n = 199 genes). (**D, E**) Type II subnetworks of hub genes showing strong interactions and loadings (highest gene-scores), denotes hub genes with strongest contribution to the change in phenotype (discriminatory power of treatments from controls). (**F-H**) Top 10-20 genes based on gene-score in each subnetwork. The colored line between genes

represents weight values from correlation matrix, low weight values (yellow) to high weight values (purple), node color indicates if DMG (yellow), both DMG-DEG (blue), DEG (grey).

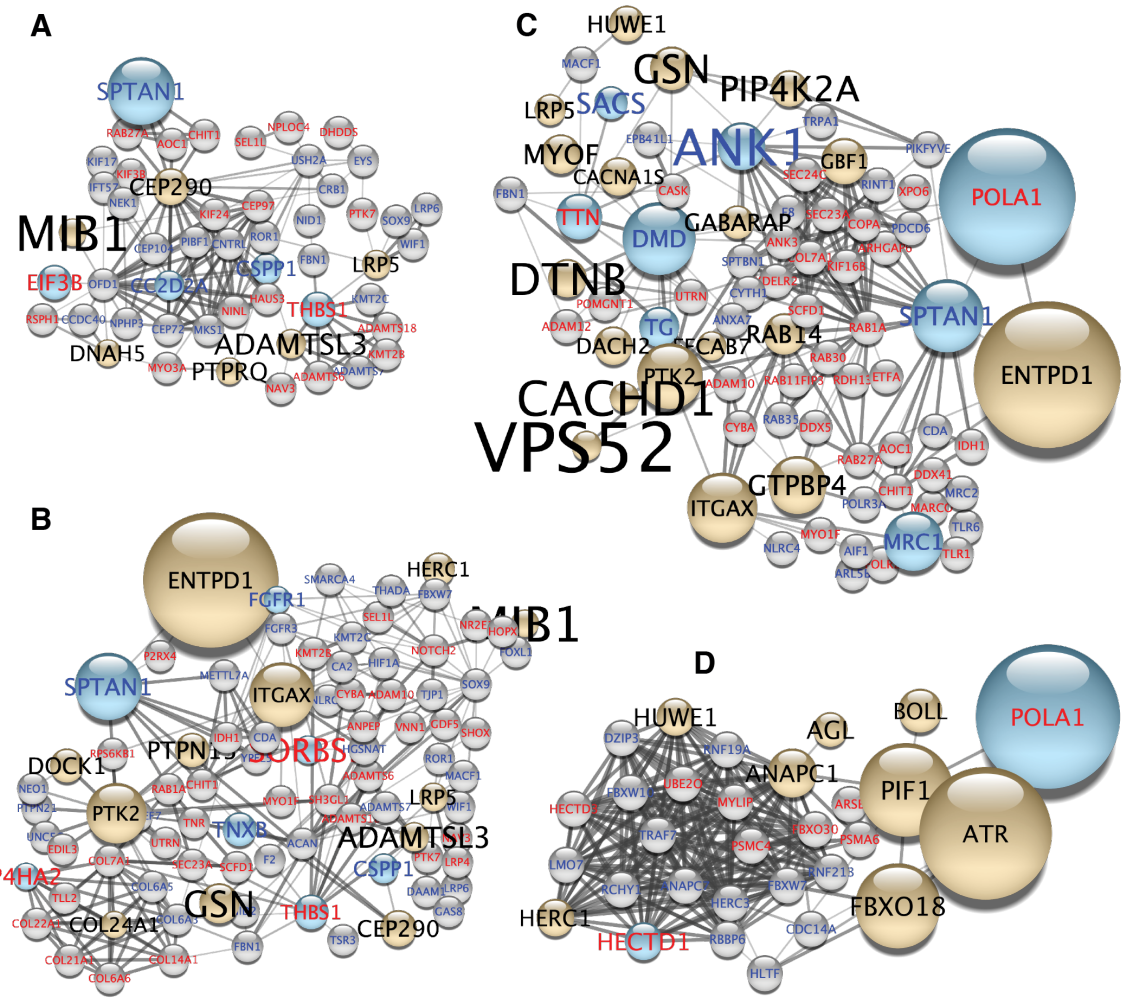

Figure 5. Predicted network-associated responses from DMGs and DEGs. Main subnetworks of hub genes retrieved from integration of DMGs and DEGs. (**A**) photoreception-phototransduction (network from StringApp without attributes: https://version11.string-db.org/cgi/network.pl?networkId=sqcU0gyKux2Y). (**B**) ECM-proteins, cell-cell adhesion and EGF-domains associated with soft tissue growth and calcification (network from StringApp without attributes: https://version11.string-db.org/cgi/network.pl?networkId=8RQKxPbg9zzZ). (**C**) Vesicle/vacuole mediated transport, Ca^{2+} metabolism and cytoskeletal protein binding associated with symbiont trafficking (network from StringApp without attributes: https://version11.string-db.org/cgi/network.pl?networkId_=Cefq2PjoZN5R). (**D**) Innate immune response associated to interpartner recognition (network from StringApp without attributes: https://version11.string-db.org/cgi/network.pl?networkId=_pZerNp9HZxM0). Larger nodes indicate key regulators or a critical target of a regulatory pathway. The line between genes represents interactions. Node color indicates if DMG (yellow), both DMG-DEG (blue), DEG (grey). Font size represents methylation (signal density variation from Methyl-IT) and font color up (red) - down (blue) regulation. Genet 1 LL to HL are shown for interpretation.

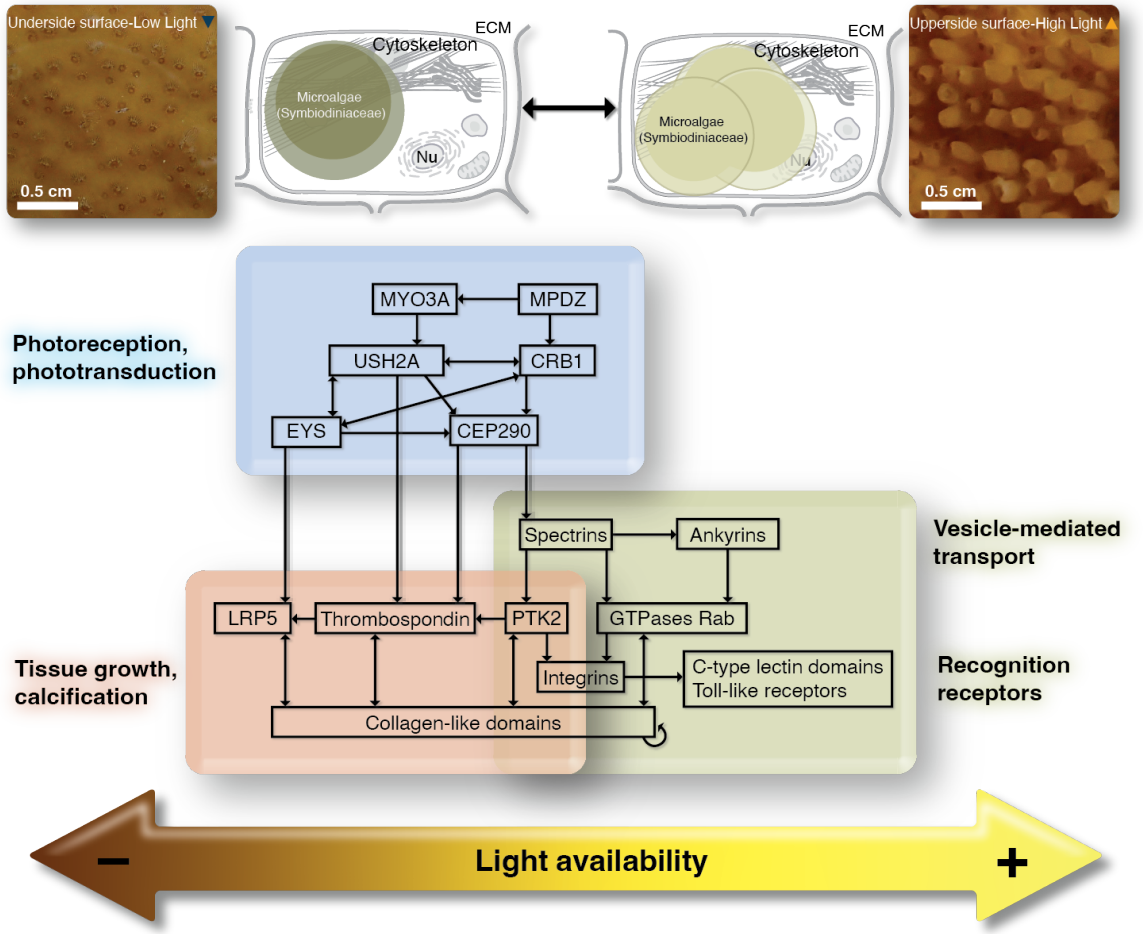

Figure 6. Predicted model for light-mediated phenotypic plasticity of structural traits in the branching coral *Acropora palmata* based on key regulators from DMGs-DEGs integrated networks. A significant change in the light environment activates photoreception mechanisms to detect cues and transduce information within cells (symbionts, cytoskeleton, extra cellular matrix-ECM, and nucleus-Nu are labeled). This activates signaling pathways to control growth, both soft tissue and skeletal growth; and in parallel, to initiate cellular transport related to symbiont recognition and changes in symbiont population densities (network from StringApp without attributes: https://version11.string-db.org/cgi/network.pl?networkId=uh6Y1lbNXqJR).

Table 1. Table of terms, definitions, and units for the structural, optical, and photosynthetic parameters used to describe phenotypes.

Traits	Parameters	Units
Structural	Corallite density at height class:	
	C_1: 0 - 1.5 mm height,	# C_{H1}-corallites cm^{-2}
	C_2: >1.5 - 3 mm height,	# C_{H2}-corallites cm^{-2}
	C_3: >3 mm height	# C_{H3}-corallites cm^{-2}
	Total polyp density	# corallites cm^{-2}
	Soluble host protein per projected area	mg protein cm^{-2}
	Chl*a* density per projected area	mg Chl*a* m^{-2}
	Algal density per projected area	#sym cm^{-2}
	Chl*a* per algal cell (Ci)	pg Chl*a* sym^{-1}
Optical	Host mass-specific absorption efficiency (a^*_M)	cm^2 mg $protein^{-1}$
	Light absorption efficiency of symbionts *in hospite* (a^*_{Sym})	m^2 sym^{-1}
	Light absorption efficiency of the holobiont (a^*_{Chla})	m^2 mg Chl*a*$^{-1}$
	Estimated Absorbance (De 675 nm)	Dimensionless
Physiological	Photosynthetic efficiency ($\boldsymbol{\alpha}$)	µmol O_2 µmol quanta
	Minimum Quantum Requirement ($\boldsymbol{\Phi}^{-1}{}_{O2}$)	mol photons $mol^{-1}{}_{O2}$
	Maximum gross photosynthetic rate per area (Pmax)	µmol O_2 m^{-2} s^{-1}
	Saturation irradiance (E_k)	µmol quanta m^{-2} s^{-1}
	Compensation irradiance (E_c)	µmol quanta m^{-2} s^{-1}
	Post-illumination respiration rate (R_L)	µmol O_2 m^{-2} s^{-1}
	Pressure over Photosystem II (Q_m)	Dimensionless